

The intriguing nature of the high energy gamma ray source XSS J12270-4859[★]

D. de Martino¹, M. Falanga², J.-M. Bonnet-Bidaud³, T. Belloni⁴, M. Mouchet⁵, N. Masetti⁶, I. Andruchow⁷,
S.A. Cellone⁷, K. Mukai⁸, and G. Matt⁹

¹ INAF - Osservatorio Astronomico di Capodimonte, salita Moiariello 16, I-80131 Napoli, Italy
e-mail: demartino@oacn.inaf.it

² International Space Science Institute (ISSI) Hallerstrasse 6 CH-3012 Bern, Switzerland
e-mail: mfalanga@issibern.ch

³ CEA Saclay, DSM/Irfu/Service d'Astrophysique, F-91191 Gif-sur-Yvette, France
e-mail: bonnetbidaud@cea.fr

⁴ INAF-Osservatorio Astronomico di Brera, Via E Bianchi 46. IT 23807 Merate (LC) Italy
e-mail: tomaso.belloni@brera.inaf.it

⁵ Laboratoire APC, Université Denis Diderot, 10 rue Alice Domon et Léonie Duquet, F-75005 Paris, France and LUTH, Observatoire de Paris, Section de Meudon, 5 place Jules Janssen, F-92195 Meudon, France
e-mail: martine.mouchet@obspm.fr

⁶ INAF Istituto Astrofisica Spaziale, Via Gobetti 101, I-40129, Bologna, Italy
e-mail: nicola.masetti@iasfbo.inaf.it

⁷ Facultad de Ciencias Astronomicas y Geofisicas, UNLP, and Instituto de Astrofisica La Plata, CONICET/UNLP, Argentina
e-mail: andru@fcaglp.fcaglp.unlp.edu.ar

⁸ CRESST and X-Ray Astrophysics Laboratory, NASA Goddard Space Flight Center, Greenbelt, MD 20771, USA and Department of Physics, University of Maryland, Baltimore County, 1000 Hilltop Circle, Baltimore, MD 21250, USA
e-mail: koji.mukai@nasa.gov

⁹ Dipartimento di Fisica, Università Roma III, Via della Vasca Navale 84, I-00146, Roma, Italy
e-mail: matt@fis.uniroma3.it

Received December 4, 2009; accepted February 15, 2010

ABSTRACT

Context. The nature of the hard X-ray source XSS J12270-4859 is still unclear. It was claimed to be a possible magnetic Cataclysmic Variable of the Intermediate Polar type from its optical spectrum and a possible 860 s X-ray periodicity in *RXTE* data. However, recent observations do not support the latter variability, leaving this X-ray source still unclassified.

Aims. To investigate its nature we present a broad-band X-ray and gamma ray study of this source based on a recent *XMM-Newton* observation and archival *INTEGRAL* and *RXTE* data. Using the *Fermi*/LAT 1-year point source catalogue, we tentatively associate XSS J12270-4859 with 1FGL J1227.9-4852, a source of high energy gamma rays with emission up to 10 GeV. We further complement the study with UV photometry from *XMM-Newton* and ground-based optical and near-IR photometry.

Methods. We have analysed both timing and spectral properties in the gamma rays, X-rays, UV and optical/near-IR bands of XSS J12270-4859.

Results. The X-ray emission is highly variable showing flares and intensity dips. The flares consist of flare-dip pairs. Flares are detected in both X-rays and UV range whilst the subsequent dips are present only in the X-ray band. Further aperiodic dipping behaviour is observed during X-ray quiescence but not in the UV. The broad-band 0.2–100 keV X-ray/soft gamma ray spectrum is featureless and well described by a power law model with $\Gamma=1.7$. The high energy spectrum from 100 MeV to 10 GeV is represented by a power law index of 2.45. The luminosity ratio between 0.1–100 GeV and 0.2–100 keV is ~ 0.8 , indicating that the GeV emission is a significant component of the total energy output. Furthermore, the X-ray spectrum does not greatly change during flares, quiescence and the dips seen in quiescence. The X-ray spectrum however hardens during the post-flare dips, where a partial covering absorber is also required to fit the spectrum. Optical photometry acquired at different epochs reveals a period of 4.32 hr that could be ascribed to the binary orbital period. Near-IR, possibly ellipsoidal, variations are detected. Large amplitude variability on shorter (tens mins) timescales are found to be non-periodic.

Conclusions. The observed variability at all wavelengths together with the spectral characteristics strongly favour a low-mass atypical low-luminosity X-ray binary and are against a magnetic Cataclysmic Variable nature. The association with a *Fermi*/LAT high energy gamma ray source further strengthens this interpretation.

Key words. Stars: binaries: close - Stars: individual: XSS J12270-4859, 1FGL J1227.9-4852 - gamma rays: stars- X-rays: binaries - Accretion, accretion disks

[★] Based on observations obtained with *XMM-Newton* and *INTEGRAL*, ESA science missions with instruments and contributions directly funded by ESA Member States and NASA, with *Fermi* a NASA mission with contributions from France, Germany, Italy,

Japan, Sweden and U.S.A. and with the *REM* Telescope INAF at ESO, La Silla, Chile

1. Introduction

Discovered as a hard X-ray source from the *Rossi XTE* slew survey (Sazonov & Revnivtsev 2004), XSS J12270-4859 (henceforth XSS J1227) was also detected as an *INTEGRAL* source and suggested to be a Cataclysmic Variable (CV) by Masetti et al. (2006) from its optical spectrum. From follow-up *RXTE* observations Butters et al. (2008) proposed a magnetic Intermediate Polar (IP) type from a possible periodic variability at a 859.6 s period. This periodicity is not confirmed in optical fast photometry (Pretorius 2009) and in a *Suzaku* X-ray observation (Saitou et al. 2009). The latter showed a peculiar X-ray variability suggesting a low-mass X-ray binary (LMXRB).

In the framework of a programme aiming at identifying the nature of newly discovered hard X-ray CV candidates we here present a broad-band gamma ray and X-ray analysis complemented with simultaneous UV coverage and new optical and near-IR photometry. A search in the recently released FERMI/LAT 1-year Point Source Catalog provides a possible identification that contributes to definitively exclude this source as a magnetic CV and to favour a LMXRB nature with an unusual variable behaviour.

2. The Fermi GeV source 1FGL J1227.9-4852

The first point source catalogue of high energy gamma ray sources detected by the Large Area Telescope (LAT) on the Fermi gamma ray Space Telescope (Fermi, formerly GLAST) mission was recently released in Jan. 2010¹. This catalogue is based on observations collected during the first 11 months of the science phase of the mission, that began on Aug. 4, 2008. It lists and characterizes all sources detected in the 100 MeV to 100 GeV range including fluxes in five energy bands as well as best fit power law spectral index.

Motivated by this first release, we searched into the catalogue for possible gamma ray counterparts and found that the source 1FGL J1227.9-4852 is at 1.21' from XSS J1227 optical position. In Fig. 1 (upper panel) we show the Fermi/LAT counts map in the range 100 MeV-300 GeV of a 12°x12° centred on 1FGL J1227.9-4852 within a maximum zenith angle of 105°. The map, with no background subtraction, is constructed from data retrieved from the Fermi Science Support Center (FSSC). The semi-major (and equal semi-minor) axis of error ellipse at 68% confidence is 3.6' and it is 6.0' at 95% confidence. There is no other significant detection within a search radius of 2.5°. 1FGL J1227.9-4852 is detected at a significance of 16.9σ with a 100MeV–100 GeV flux of $3.95 \pm 0.44 \times 10^{-11}$ erg cm⁻² s⁻¹ and best fit power law index of 2.45±0.07. 1FGL J1227.9-4852 is detected in four out of five LAT bands from 100 MeV up to 10 GeV, with listed fluxes that are the integral photon fluxes for the source in the given energy bands computed via the maximum likelihood method, that takes into account the various backgrounds, contributions from other sources, instrument response function and exposure time. The optical position is shown together with the 95% confidence error ellipse as reported in the Fermi/LAT 1-year Point source catalogue. The positional coincidence of both sources is a strong indication that XSS J1227 could be the counterpart of 1FGL J1227.9-4852.

Variability over a 11-month interval is also provided for each catalogued source. The 100 MeV-100 GeV light curve of 1FGL J1226.9-4852 binned with a time interval of one month does not reveal any variability within statistical uncertainty. The

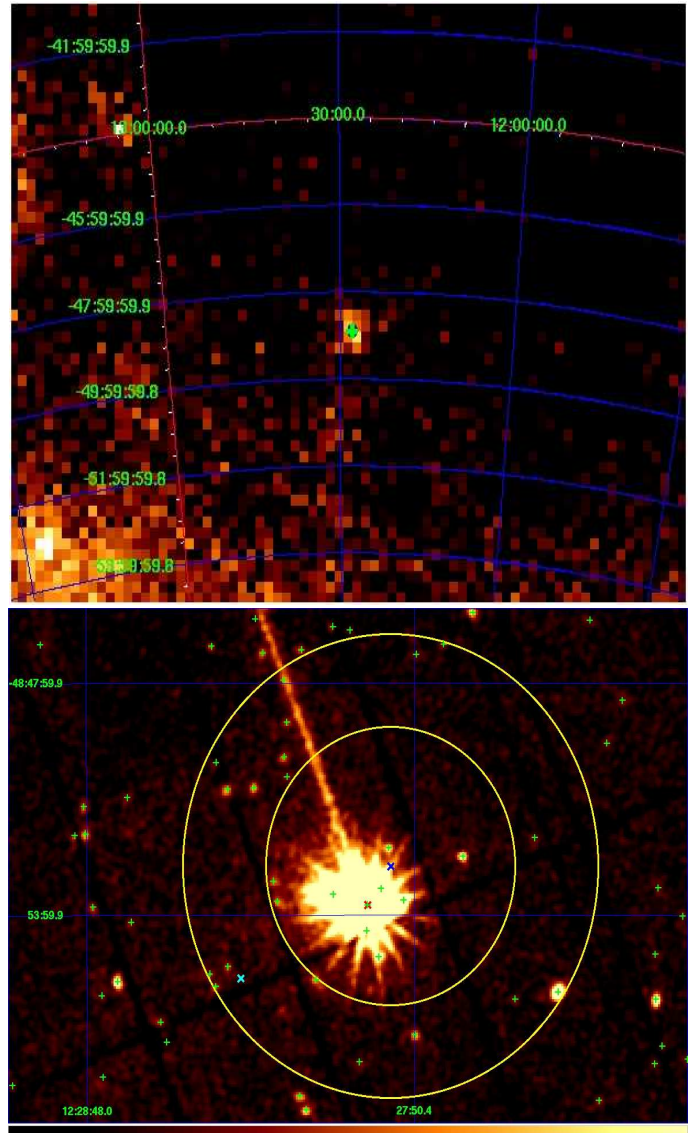


Fig. 1. *Upper panel:* The counts map in the range 100 MeV-300 GeV of a 12°x12° region centred at the optical position of XSS J1227 (marked with a green cross) together with the 95% confidence region (green circle) of the *Fermi*/LAT source 1FGL J1227.9-4852. *Lower panel:* The combined EPIC pn, MOS1 and MOS2 image in the 0.2–12 keV range centred on XSS J1227 (red cross) together with the position (blue cross) and 68% and 95% confidence regions (yellow circles) of the *Fermi*/LAT source 1FGL J1227.9-4852. Sources detected in the EPIC cameras using the standard *XMM-Newton* SSC pipeline are also displayed with green crosses. The position of the radio source SUMSS J122820-485537 is also reported (cyan cross). The bright strip is an artifact.

variability index, based on a χ^2 -test of deviation of the flux in 11 monthly time bins, is 3.8. Hence, the source is at a constant flux level on a long term (month) timescale. A detailed search for shorter time variations is deferred in a future work.

3. Observations and data reduction

Here we report our new observation acquired with *XMM-Newton* as well as the publicly available *INTEGRAL* data. Archival *RXTE* observations were also retrieved to complement the spec-

¹ http://fermi.gsfc.nasa.gov/ssc/data/access/lat/1yr_catalog/

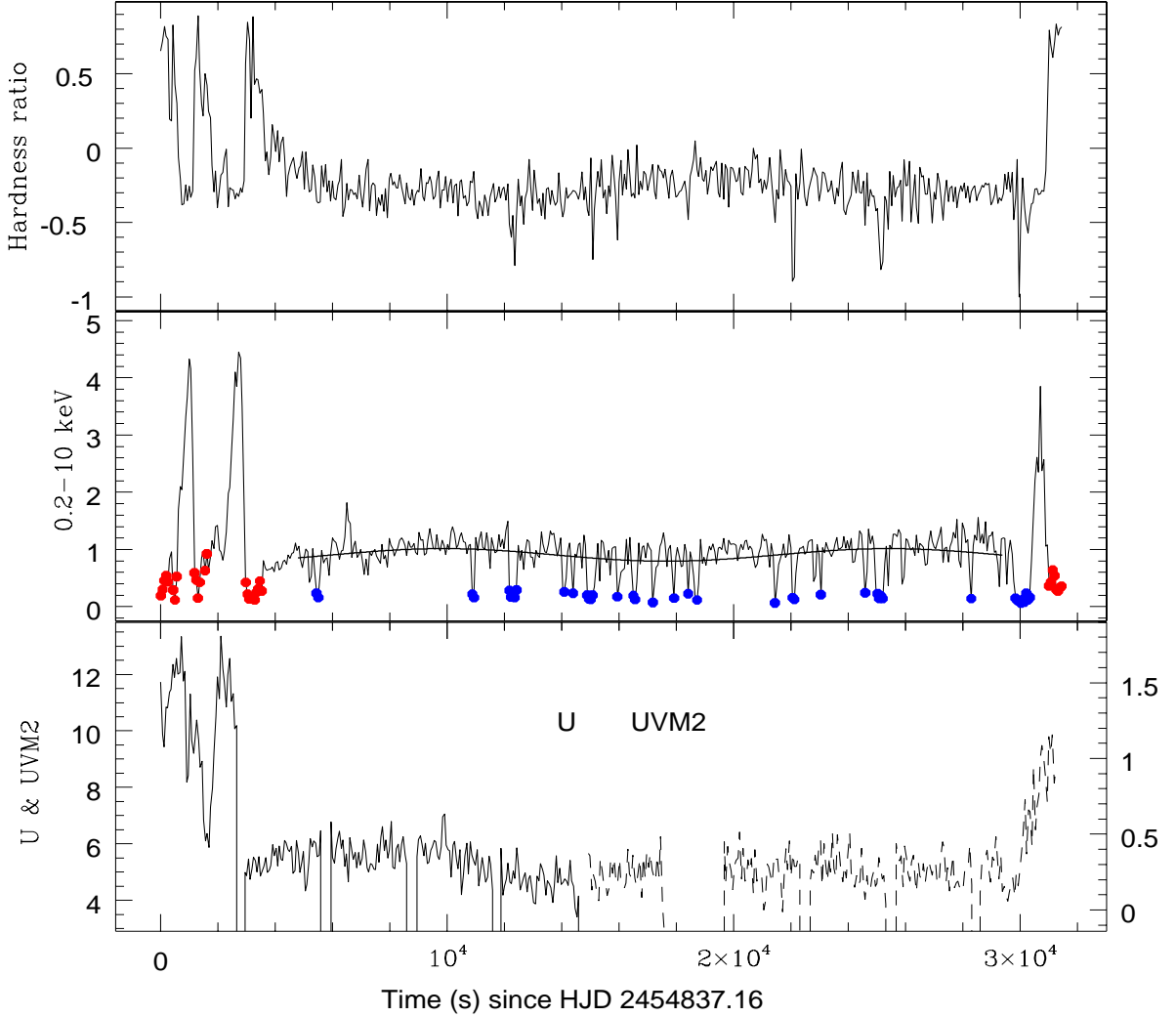


Fig. 2. *Bottom:* OM-U (solid line) and OM-UVM2 (dashed line) background subtracted light curves. Ordinates at the left report the OM-U count rate and at the right the OM-UVM2 band count rate. Gaps are due to the OM fast mode windows. *Middle panel:* EPIC-MOS (MOS1 and MOS2) combined light curve in the 0.2–10 keV band. A sinusoidal function at a period of 244.5 min is also shown. Red points refer to hard dips whilst blue points refer to soft dips that are reported in Fig. 4 (see also text). *Top:* Hardness ratio defined as $[H-S/H+S]$ between 2–10 keV and 0.2–2 keV bands from combined EPIC-MOS light curves. A bin size of 60 s is adopted for clarity in the three panels.

tral and timing analysis of this source. We further present optical and near-IR data acquired at the *CASLEO* and *REM* telescopes.

The summary of the observations of XSS J1227 is reported in Table 1.

3.1. The XMM-Newton observations

The *XMM-Newton* observation (OBSID: 0551430401) was carried out on Jan.5, 2009 with the EPIC cameras (pn: Strüder et al. (2001) and MOS: Turner et al. (2001)) operated in imaging full window mode using the thin filters and with the OM (Mason et al. 2001) operated in fast window mode using sequentially the U (3000–3800 Å) and UVM2 (2000–2800 Å) filters for ~ 13.3 ks each.

The data were processed using the standard reduction pipelines and analyzed with the SAS 8.0 package using the latest

calibration files. We used a 34'' (37'') aperture radius to extract EPIC-pn (EPIC-MOS) light curves and spectra from a circular region centered on the source and from a background region located on the same CCD chip. In order to improve the S/N ratio, we filtered the data by selecting pattern pixel events up to double with zero quality flag for the EPIC-pn data, and up to quadruple pixel events for the EPIC-MOS data. The average background level of the EPIC cameras was low for all the duration of the observation, with the exception of a flaring activity, lasting ~ 4800 s and occurring at the end of the EPIC-pn exposure. This flare does not significantly affect the light curves, but we conservatively exclude that period in the extraction of the spectra.

Considering the possible association of XSS J1227 with the high energy gamma ray source 1FGL J1227.9-4852, we also inspected the source catalogue detected in the EPIC cameras, produced by the standard *XMM-Newton* Survey Science Center (SSC) pipeline. In Fig. 1 (lower panel), the combined EPIC

Table 1. Summary of the observations of XSS J1227.

Telescope	Instrument	Date	UT (start)	Exposure time (s)	Net count rate (counts s ⁻¹)
<i>XMM-Newton</i>	EPIC-pn	2009-01-05	16:09	30 002	2.86 ± 0.01
	EPIC-MOS		15:46	31 504	0.97 ± 0.04
	OM-U		15:56	13 298	6.35 ± 0.04
	OM-UVM2		20:05	13 296	0.36 ± 0.01
<i>INTEGRAL</i>	IBIS/ISGRI			~ 750 000	0.14 ± 0.05
<i>RXTE</i>	PCA	2007-11-28	16:13	6 784	1.3±0.1
		2007-11-28	22:02	3 616	2.6±0.1
		2007-11-29	02:04	1 168	1.4±0.2
		2007-11-29	04:35	22 832	1.43±0.05
		2007-11-29	12:06	14 416	1.28±0.07
Telescope	Instrument	Date	UT (start)	Exposure time (s)	Number exposures
<i>REM</i>	ROSS-V	2009-03-18	05:46	60	93
	ROSS-V	2009-03-19	05:54	60	175
	ROSS-V	2009-03-20	05:54	60	185
	REMIR-J	2009-03-18	05:47	75	30
	REMIR-J	2009-03-19	05:54	75	75
	REMIR-J	2009-03-20	05:54	75	83
<i>CASLEO</i>	B	2008-07-07	00:28	30	158

* Net exposure times except for the *INTEGRAL* observations.

pn, MOS1 and MOS2 image in the 0.2–12 keV centred on XSS J1227 is shown together with the *Fermi* 68% and 95% confidence regions. Although there are a number of X-ray sources within these regions, these are much fainter than XSS J1227. Most are found at a count rate (EPIC pn) much lower than 0.04 cts s⁻¹, with only one source at 0.26 cts s⁻¹ (corresponding to a 0.2–12 keV flux of 8.6×10^{-13} erg cm⁻² s⁻¹), located at 1.0' north-east from XSS J1227. We therefore conclude that there are no other favoured X-ray counterparts than XSS J1227.

Background subtracted OM-*U* and OM-*UVM2* light curves were obtained with a binning time of 10 s. The average count rates were 6.35 counts s⁻¹ in the *U* band and 0.36 counts s⁻¹ in the *UVM2* band, corresponding to instrumental magnitudes $U = 16.5$ and $UVM2 = 17.3$ and to average fluxes 8.2×10^{-16} erg cm⁻² s⁻¹ Å⁻¹ and 5.3×10^{-16} erg cm⁻² s⁻¹ Å⁻¹, respectively.

Heliocentric corrections were applied to the EPIC and OM arrival times.

3.2. The INTEGRAL observations

The *INTEGRAL* IBIS/ISGRI (Ubertini et al. 2003; Lebrun et al. 2003) hard X-ray data of the source were extracted from all pointings within 12° from the source positions, spanning from March 2003 to October 2007. The total effective exposure times is ~ 750 ks (651 pointings). To study the weak persistent X-ray emission, the time averaged ISGRI spectrum was obtained from mosaic images in five energy bands, logarithmically spaced between 20 and 100 keV. Data were reduced with the standard OSA software version 7.0 and, then, analyzed using the algorithms described by Goldwurm et al. (2003).

3.3. The RXTE observations

Archival *RXTE* (Bradt et al. 1993) observations acquired in November 2007 and published in Butters et al. (2008) were retrieved to search for the peculiar behaviour detected in our *XMM-Newton* observation, about one year later. The *RXTE*/PCA exposures amount to a total effective time of 48.8 ks (see Table 1). This is remarkably longer than that reported in Butters et al. (2008). To allow a direct comparison, the *RXTE* data reduction and analysis was performed with a procedure similar to that described in Butters et al. (2008).

3.4. The optical and near-IR photometry

XSS J1227 was observed for one night on July 7, 2008 at the 2.15 m telescope at the Complejo Astronomico el Leoncito, *CASLEO*, in Argentina, equipped with a direct CCD camera. B band time-series photometry was acquired for 2.64 h adopting 30 s exposure times for each image. Data reduction was performed using standard *iraf* routines. The B band photometry was however affected by spurious light variable with time of unknown nature. We therefore did not apply dark and sky corrections. Aperture photometry was obtained for the star and several (ten) comparison stars in the field. Hence, differential photometry was obtained by dividing the target count rates with the average count rate of the comparison stars. The error associated to each data point was less than 0.05 mag

XSS J1227 was further observed on March, 18, 19 and 20, 2009 with the 0.5 min Rapid Eye Mount (*REM*) robotic telescope at the ESO, La Silla observatory in Chile (Zerbi et al. 2004), equipped with the ROSS (Tosti et al. 2004) and REMIR (Conconi et al. 2004) cameras that simultaneously covered the V and J photometric bands. Exposure times of individual images were 60 s in the V band. The J band photometry was carried out using a dithering of five images on the source, each of 15 s exposure. A sky J band image was also sequentially acquired for

each set of dithered images. The source was observed for 1.8 h, 3.4 h and 3.7 h during the three consecutive nights. Data reduction was also performed using *iraf* routines including flat field and dark corrections for the V band images. The J band images are routinely pre-reduced by the *REMIR* pipeline that provides sky subtracted and de-biased images. Aperture photometry was carried out using *daophot* routine. Relative photometry was obtained by using several comparison stars in the field. Flux ratios were obtained by dividing the target counts by the combination (weighted mean) of five reference stars. Errors on each data points are ~ 0.09 mag and 0.3 mag in the V and J band respectively. In the latter band the source was faint and not always detected providing a badly sampled light curve. Average V band magnitudes were: 16.70, 15.85 and 17.31 mag and the average J band magnitudes were 16.14, 15.75 and 16.53 mag during the three consecutive days. These were derived by comparing the photometry of the reference star HD 108433 in the target field. A comparison with the optical spectrum acquired by Masetti et al. (2006) indicates that XSS J1227 was about at the same optical level. Furthermore from a comparison with J-band 2MASS magnitude ($J=15.73$ mag), the source is found at a comparable level.

The flux ratios of individual nights were converted to fractional intensities dividing them by the corresponding nightly mean. Heliocentric corrections were also applied to all photometric data sets.

4. Results

4.1. The X-ray variability of XSS J1227

The EPIC-pn and MOS light curves were extracted in the energy range 0.2–12.0 keV and binned in 20 s time intervals. In all instruments we observe similar temporal behaviour. Hence, due to the slightly shorter exposure of the EPIC-pn camera we discuss the variability observed in the EPIC-MOS cameras.

The X-ray light curve shows two strong events at the beginning of the exposure where the count rate reaches a peak intensity ~ 4.6 times the persistent level. The second occurs ~ 30 min after the first one. A third event, covered only by the EPIC-MOS cameras, is also observed at the end of the exposure, ~ 7.3 hr after the second one. We also detect similar events in the *OM* – *U* and *OM* – *UVM2* bands (Fig. 2), which therefore are regarded as real. We will refer to them as “flares”. These are remarkably similar to each other in temporal evolution and intensity. The rise is less steep than the decay and structured, consisting of a sequence of peaks before reaching the maximum intensity (see enlargement in Fig. 3). The third flare is even more structured. The decay to quiescent level is also not smooth, with a peak occurring ~ 1 min later than the maximum (best seen in the first two flares) and lasting ~ 2.3 min, followed by a decrease of the count rate below the quiescent persistent level (“dip”). The duration of the flares are 11.5 min and 12 min and 9.2 min, respectively. The third flare is also preceded by a rather broad dip. An additional weak event is observed ~ 1.8 hr after the beginning of the MOS exposure with peak intensity 2 times the quiescent flux and duration of 3.9 min. Also for this event a weak and short dip is detected that however does not reach the low count rate level observed in the others.

We here define the hardness ratio as: $HR = [H-S/H+S]$, where H and S are the count rates in the 2–10 keV and 0.2–2 keV bands, respectively. Their temporal behaviour, shown in Fig. 2, demonstrates that the flares are not characterized by strong changes in the spectral shape, contrary to the dips associated to them, that show instead a hardening of the spectrum. Also,

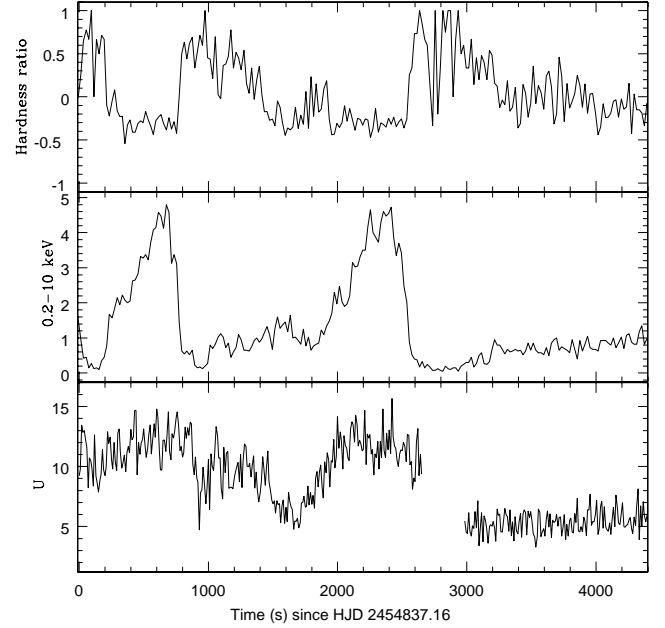


Fig. 3. Enlargements of the activity phase at the beginning of the *XMM-Newton* observation in the U band (bottom), the X-ray 0.2–10 keV band together with hardness ratios defined in the text (top). Bin size is 20 s.

pronounced non-periodic dips characterise the quiescent persistent emission. The count rate changes by a factor of ~ 3 in the strongest dips. Their occurrence intensifies between 2.9 hr and 7.9 hr after the beginning of the MOS observation. The dips have variable length ranging from 2 min to 5 min for the more pronounced dips. Hardness ratios (Fig. 2) do not greatly change, except in a few intense dips where a softening is observed. Hence, the dips observed in quiescence and those associated to the flares have different origin.

This peculiar behaviour is best seen in the intensity versus hardness ratio (HR) diagram as depicted in Fig. 4. Different locii can be identified: hard dips (shown in red) with hardness ratio $HR > 0.3$; soft dips (shown in blue) with $HR < 0$ and count rate < 0.3 cts s^{-1} ; quiescence with count rate > 0.3 cts s^{-1} but < 2 cts s^{-1} and $-0.7 < HR < 0.3$ (shown in green) and the flares with count rate > 2 cts s^{-1} and $-0.4 < HR < 0$. The diagram reveals similar spectral shape between quiescence and flares. The spectrum instead is harder during the dips after the flares but not during those occurring in quiescence. The red and blue colours refer to the points also reported in Fig. 2. Since the quiescence prior the first flare is not observed and given that the dip preceding it shows similar spectral behaviour as the post-flare dips, it is plausible that this first flare is also preceded by another event. If it is the case, it might be concluded that only the post-flare dips show spectral hardening with respect to all other temporal features observed in the X-ray light curve.

We inspected flare fluence (total flare counts), duration and total flux in the dips associated to them. The ratio of flare fluence and count rate deficiency is ≥ 8 in the first event and, remarkably, ~ 7.5 in the second and third. Note that the dip associated to the first flare is less evident and hence more difficult to isolate; it lasts less than the others, possibly because of the superposition or closeness of the second flare. The length of the dips increases with the duration of the flare, the second flare and associated dip

being the longest. This suggests that flares and dips are correlated and hence the events consist of flare-dip pairs.

Variations in the soft and hard X-ray bands during flares were also inspected by computing the cross-correlation function (CCF) between the soft, 0.2–2 keV and hard 2–10 keV bands. This is shown in Fig. 5 (bottom panel) for the portion of the light curve that includes the first two flares. The CCF peaks at zero lag, but is slightly asymmetric towards positive lags. Taking as reference the soft band, the CCF suggests that the hard X-ray variations on timescales ≥ 300 s lag the soft ones. This can be also seen from the large amplitude variations of HRs, shown in Fig. 3, during and immediately after the dips.

We also detect a weak (4%) long-term quasi-sinusoidal trend in the quiescent flux. The length of the MOS exposure however does not allow us to determine the period as we obtain similar χ^2 fitting a sinusoid with periods between 200–280 min. To illustrate this we also show in Fig. 2 a sinusoidal function at the fixed period of 4.32 h found in the optical photometry (see Sect. 3.3).

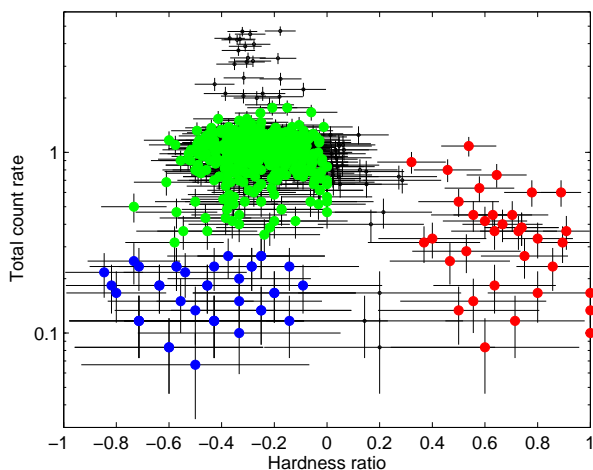


Fig. 4. Diagram of total MOS intensity versus hardness ratio in the 0.2–2 keV and 2–10 keV bands. Green points represent quiescence (not reported in Fig. 2 for clarity), red points are the dips observed after the flares and the blue points represent the dips observed during quiescence. Flares are denoted with black points.

This peculiar X-ray variability led us to compare the *XMM-Newton* light curve with that observed with *RXTE* in Nov. 2007, as Butters et al. (2008) neither show it nor report any atypical behaviour. The *RXTE* PCA light curve in the 2–20 keV band is displayed in Fig. 6 with similar sampling and temporal scale as the EPIC MOS one. Also in these data flares and dips are observed with similar timescales as in our data. In particular a series of flares are observed ~ 20 ks after the start of the *RXTE* pointing, each of them lasting ~ 8 –12 min. The duration of this active period cannot be determined due to the gaps in the data. It is however clear that a relatively long (≥ 5.3 hr) quiescent period follows the active phase, during which dips, lasting ~ 6 –13 min, are detected. This quiescent period has been Fourier analysed in order to detect the 859.6 s periodicity reported by Butters et al. (2008) but we did not find any significant peak. Furthermore and as apparent from Fig. 6, the data are too noisy to detect low frequency variations.

We therefore conclude that XSS J1227 is a persistent X-ray source with flaring and dipping characteristics. This is fur-

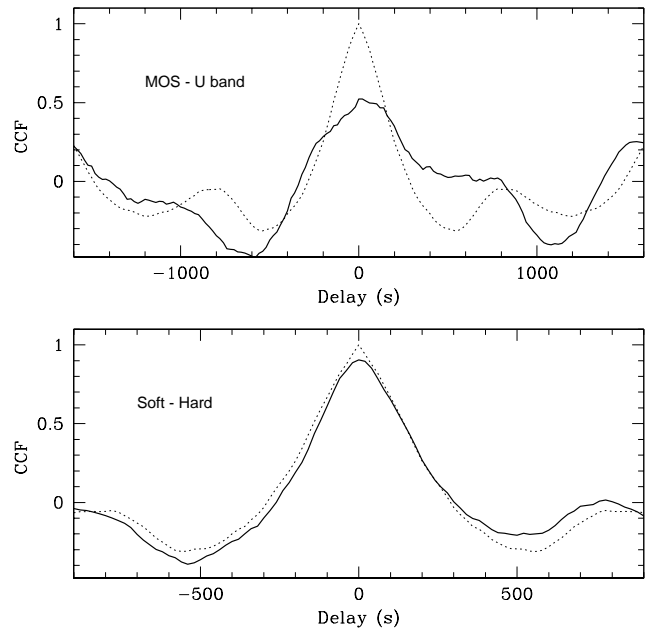


Fig. 5. *Bottom:* The CCF between the hard (2–10 keV) and soft (0.2–2 keV) light curves during the first two flares (thick line) together with the auto-correlation function of the soft band light curve, taken as reference light curve (dotted line). *Top:* The CCF between the U band and 0.2–10 keV MOS light curves (thick line) together with the auto-correlation function (dotted line) of the MOS light curve.

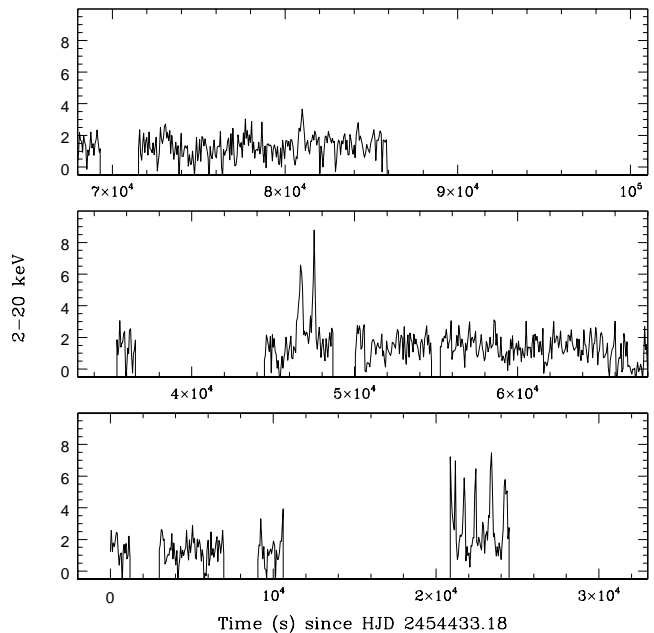


Fig. 6. The *RXTE* PCA light curve in the 2–10 keV band as observed in 2007. A bin size of 60 s and a similar temporal scale as the *XMM-Newton* EPIC light curve are adopted for clarity.

ther corroborated by a *Suzaku* observation carried out in August 2008, recently reported by Saitou et al. (2009).

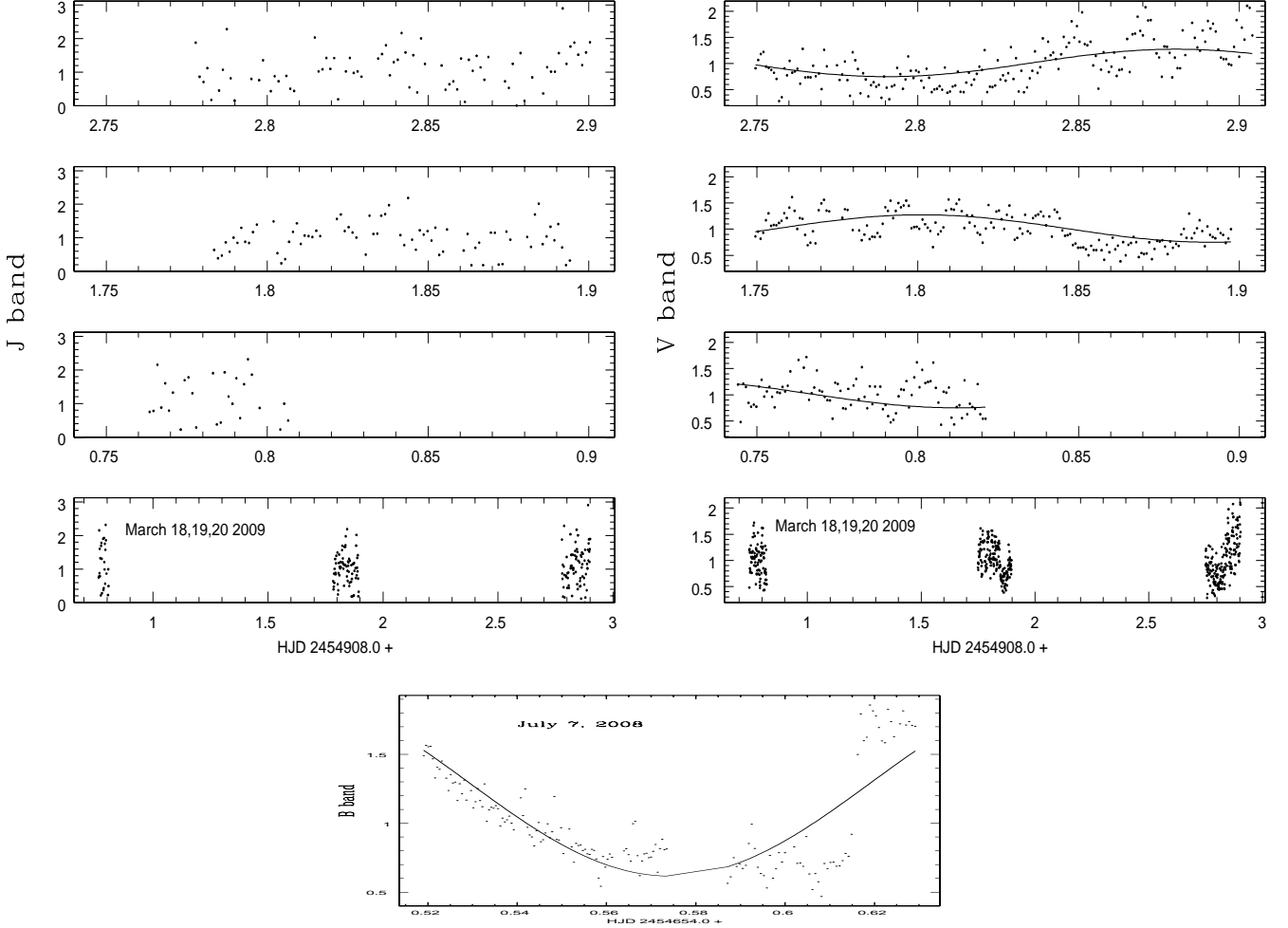


Fig. 7. *Bottom:* The B band light curve observed in 2008. *Top right panels:* The V band photometry during the three consecutive nights in March 2009. *Top left panels:* The near-IR light curves during the same nights in 2009. The optical light curves are also shown together with a sinusoidal function at a period of 259 min (see text for details).

4.2. The UV variability of XSS J1227

The flares detected in the ultraviolet, U and UVM2 bands, have also similar peak intensities reaching ~ 3 times the quiescent persistent level (Fig. 2). They however appear to last longer than the X-ray flares, though we lack coverage of the quiescent level before onset of the first UV flare and of the decay to quiescence of the second flare. Also, the U band light curve is highly structured between the two events, whilst it is not so in the X-rays. We find that the decay to quiescence of the first flare in the U band occurs 1.2 min later than the X-rays and the rise of the second flare occurs 1.8 min earlier than the X-rays (see enlargement in Fig. 3). Similarly, the third flare observed at the end of the *XMM-Newton* observation starts earlier in the UVM2 band (Fig. 2) and, although only the rise is covered, it also seems to last longer than the X-ray flares. Worth noticing is that the weak X-ray flare after the first two larger ones, is not detected in the ultraviolet (U band).

We also computed the CCF between the U and X-ray, 0.2–10 keV, light curves covering the first two flares taking as reference the X-ray light curve (see Fig. 5 upper panel). Also in this case the CCF peaks at zero lag but it is strongly asymmetric towards positive lags, with major differences at lags ≥ 300 s up to 900 s. Hence the UV variations are delayed with respect to the

X-rays and this could be understood with a longer duration of the UV flares.

The U band magnitude at flare peak is $U_{\text{peak}} \sim 15.3$ mag and at quiescence $U_{\text{quie.}} \sim 16.5$ mag. In the UVM2 band, we observe the third flare at $UVM2_{\text{peak}} \sim 15.3$ mag while at quiescence $UVM2_{\text{quie.}} \sim 17.3$ mag. The magnitude differences are then 1.2 ± 0.1 mag and 2.0 ± 0.3 mag in the U and UVM2 bands, respectively. Assuming that all flares in each band reach similar intensity, then $(UVM2 - U)_{\text{peak}} \sim 0.0$ and $(UVM2 - U)_{\text{quie.}} \sim 0.8$, implying that flares are blue.

Furthermore, the X-ray dips occurring in quiescence do not have a counterpart in the UV range. This suggests that the dipping behaviour is related to the regions where the X-rays are emitted. The quiescent UV flux seems instead to be variable on timescales of hours resembling the weak quasi-sinusoidal variation seen in the X-rays, but we are unable to determine any periodicity due to the short coverages in the two bands.

4.3. The optical and near-IR variability

We analysed the B band *CASLEO*, the V and J band *REM* light curves shown in Fig. 7. All of them show large amplitude variations ($\sim 40 - 50\%$) on timescales of hours as well as ~ 20 -

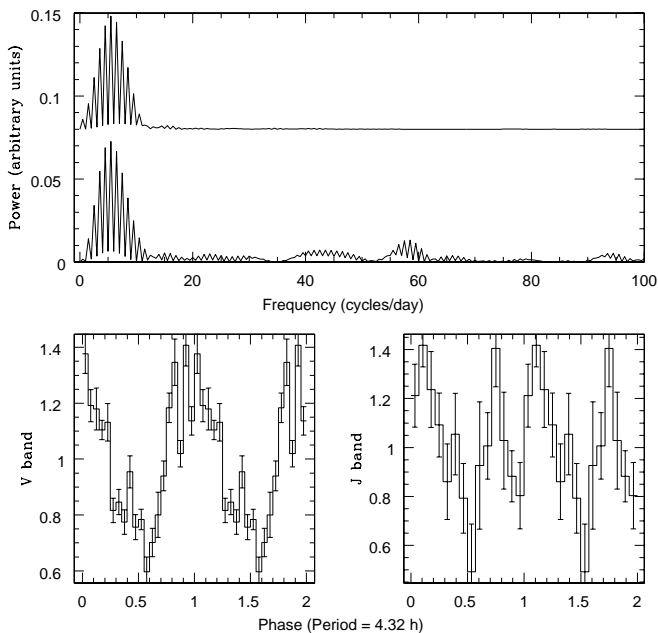


Fig. 8. *Top* The Fourier spectrum of the V band photometry acquired in March 2009 together with the synthetic spectrum obtained with a sinusoidal function fitted to the V band data at a 4.32 hr period. The latter is shifted in ordinates for clarity. *Bottom:* Folded V (left) and J (right) band light curves at this period.

Table 2. Spectral fit parameters to the broad-band 0.2–100 keV spectrum of XSS J1227.

Model	Power law	COMPTT	Bremsstrahlung
N_H (10^{21} cm^{-2})	0.98 ± 0.04	0.95 ± 0.05	0.6 ± 0.03
Γ	1.7 ± 0.02	–	–
kT_{seed} (keV)	–	0.08 ± 0.02	–
kT_{plasma} (keV)	–	53^{+27}_{-17}	–
τ	–	$1.1^{+2}_{-0.5}$	–
kT_{Brems}	–	–	12.6 ± 0.6
$\chi^2/\text{d.o.f.}$	976/915	982/913	1116/914
$\text{Flu}_{0.2-100\text{keV}}^{\text{abs,*}}$	4.2 ± 0.2	3.8 ± 0.5	1.6 ± 0.4
$\text{Flu}_{0.2-100\text{keV}}^{\text{unabs,*}}$	4.5 ± 0.9	4.1 ± 1.0	1.9 ± 0.9

* in units of $10^{-11} \text{ erg cm}^{-2} \text{ s}^{-1}$

30% short term (tens of minutes) variability. The J band data are rather poor in statistics and cannot be used to search for periodicities. We then Fourier analysed only the B and V band light curves. These do not reveal any coherent signal at the purported period of 859.6 s, thus confirming the results obtained by Pretorius (2009). On the other hand, in the *REM* optical data we find significant signal at $\nu \sim 6 \text{ day}^{-1}$ (see Fig. 8). A sinusoidal fit to the *REM* V band light curve covering the three nights gives a best fit period of $4.32 \pm 0.01 \text{ h}$. A comparison of the synthetic Fourier spectrum with that of the observed light curve is also shown in Fig. 8. The same period is used to fit the low frequency variability observed in the B band *CASLEO* photometry. The modulation amplitude is $\sim 50\%$ in the B band July 2007 data and is $\sim 40\%$ in the V band March 2009 observations. The

folded light curves in the V and J bands at this period are also shown in Fig. 8. Despite the low statistics of the near-IR data, both light curves show a pronounced minimum at similar phases. A possible secondary minimum seen in the J-band could also be present in the V data, but better data are needed to study the near-IR variability. The weak quasi-sinusoidal variability detected in the *XMM-Newton* quiescent X-ray light curve is consistent with this period, suggesting a possible link with the binary orbit in the X-ray data.

Furthermore, the B and V band light curves detrended from this periodicity show large amplitude ($\sim 40\%$) variability on a timescale of $\sim 25\text{--}30 \text{ min}$ but this is not found to be coherent. We therefore conclude that this short term variability is non periodic and hence of flickering type. This is further supported by the photometric variability observed in April 2008 and reported by Pretorius (2009), showing different behaviour from night to night. Since the nightly coverage of the present data is at most 4.7 hr and due to the lack of simultaneous X-ray data, it is difficult to assess whether the large amplitude short-term optical variations are linked to the flaring activity observed in the X-ray and UV bands. We note however that the UV flares last at least 1500 s and hence it cannot be excluded that the optical band is also affected by similar flaring behaviour.

5. The X-ray spectrum of XSS J1227

To investigate the broad-band spectrum and its variability we used the *XMM-Newton* EPIC-pn, the *RXTE* PCA and *INTEGRAL* ISGRI data with the spectral analysis package XSPEC version 12.4.

5.1. The broad-band X-ray spectrum

The extracted *XMM-Newton* EPIC-pn grand-average spectrum between 0.2–10 keV is featureless with no sign of an iron complex at 6–7 keV. The *RXTE* PCA average spectrum extracted between 3–20 keV also does not require any iron line and does not show any high energy cut-off.

Before combining the different data sets we checked whether the source was in a different luminosity state during the five *RXTE* segments and the *XMM-Newton* observation that were separated by about one year. Due to the lack of spectral features, we adopted an absorbed power law. The absorption is not needed to fit the *RXTE* PCA spectra; we find similar results fixing the absorption to the value found from the *XMM-Newton* data. The results are reported in Table 3. Both the quiescent flux levels and power law indices are about the same in 2007 and 2009. Also, during both observations the time spent by the source in quiescence is longer than during flares: $\sim 18\%$ during the *XMM-Newton* pointing and $\sim 12\%$ during the *RXTE* observation. As shown in Sect. 4.2, the spectrum does not change during the flares. This indicates that the source was in a similar luminosity and spectral state at the two epochs.

We therefore combined the *XMM-Newton* EPIC-pn, *RXTE* PCA and *INTEGRAL* ISGRI data to study the broad-band spectrum. We used in our fits a simple absorbed power law, an absorbed cut-off power law and a Bremsstrahlung model. For all the fits we fixed the normalization constant to the *XMM-Newton* data and the normalizations of the PCA and ISGRI data were ~ 1.3 . This also indicates that no strong flux variations occurred. We find that a power law fits well the data as the inclusion of a cut-off is not statistically significant with a lower limit of 55 keV. A thermal bremsstrahlung model gives a much lower fit quality.

Table 3. Spectral fit parameters of time-resolved spectra of XSS J1227 using an absorbed power law.

Model	EPIC-pn	EPIC-pn	EPIC-pn	EPIC-pn	EPIC-pn
	Dip	Out-of-dip	Flare	Quiescence	Post-flare dip
N_H (10^{21}cm^{-2})	1.1 ± 0.3	0.97 ± 0.04	0.78 ± 0.11	0.94 ± 0.04	1.06 ± 0.06
Γ	1.7 ± 0.1	1.59 ± 0.02	1.59 ± 0.02	1.58 ± 0.02	1.32 ± 0.3
N_H (10^{22}cm^{-2})	–	–	–	–	$6.11^{+2.4}_{-1.9}$
C_F	–	–	–	–	$0.86^{+0.106}_{-0.11}$
$\chi^2/\text{d.o.f.}$	44/55	932/843	245/277	915/852	25/24
$\text{Flux}_{2-10\text{keV}}^{\text{abs,*}}$	0.16 ± 0.03	1.0 ± 0.2	2.6 ± 0.1	0.9 ± 0.2	0.8 ± 0.1

	PCA Obs. 1	PCA Obs. 2	PCA Obs. 3	PCA Obs. 4	PCA Obs. 5
	Quiescence	Flare	Quiescence	Quiescence	Quiescence
Γ	1.9 ± 0.2	1.7 ± 0.1	1.6 ± 0.3	1.7 ± 0.1	1.7 ± 0.1
$\chi^2/\text{d.o.f.}$	21/37	27/37	20/37	35/37	22/37
$\text{Flux}_{2-10\text{keV}}^{\text{abs,*}}$	1.3 ± 0.2	1.6 ± 0.2	1.2 ± 0.3	1.3 ± 0.2	1.2 ± 0.2

* in units of $10^{-11} \text{erg cm}^{-2} \text{s}^{-1}$

Though more physically motivated, the Comptonization model `COMPTT`, where soft seed photons with kT_{seed} are comptonized by a hot plasma at kT_{plasma} with optical depth τ does not give constrained parameters due to the lack of a cut-off at high energy in our data. An additional blackbody (`BBODY`) is also not required by our data. The results of the fits are reported in Table 2.

We therefore conclude that the broad-band featureless spectrum of XSS J1227 is well described by a weakly absorbed power law as shown in Fig. 9. The hydrogen column density $\sim 1 \times 10^{21} \text{cm}^{-2}$ is compatible with that in the direction of the source ($1.2 \times 10^{21} \text{cm}^{-2}$) (Dickey & Lockman 1990), thus indicating an origin in the interstellar medium.

5.2. Time-resolved X-ray spectra

The intensity vs hardness ratio diagram shows that the source does not significantly change its spectral shape during flares, during the quiescent persistent emission and during dips in quiescence. It instead changes during the dips observed immediately after the flares. We then extracted the *XMM-Newton* EPIC-pn spectra during the flares (flare spectrum), their associated dips (post-flare dip spectrum) as well as during the quiescent dips (dip spectrum), the quiescence including (quiescence spectrum) and excluding them (out-of-dip spectrum). To fit these data we used an absorbed power law as discussed above. As expected all spectral fits provide similar power law index within errors, except for the post-flare dip spectrum that gives $\Gamma = 0.22^{+0.13}_{-0.12}$ but $\chi^2/\text{d.o.f.} = 49/26$. The fit of this spectrum improves by including a partial covering absorber with 86% covering fraction and $N_H = 6.1 \times 10^{22} \text{cm}^{-2}$. With this component the power law index increases to $\Gamma = 1.3$ and is consistent within errors with that found in the other fits. Furthermore, the flare spectrum shows hints of an emission feature at the iron complex. However, the inclusion of a gaussian line, found at 6.2 keV, gives a slight though not significant, improvement to the fit. The results are reported in Table 3 and shown in Fig. 10.

6. The combined X-ray and gamma ray spectrum

Considering the possible association with 1FGL J1227.9-4852, we have combined the fluxes in the four *Fermi* LAT bands and

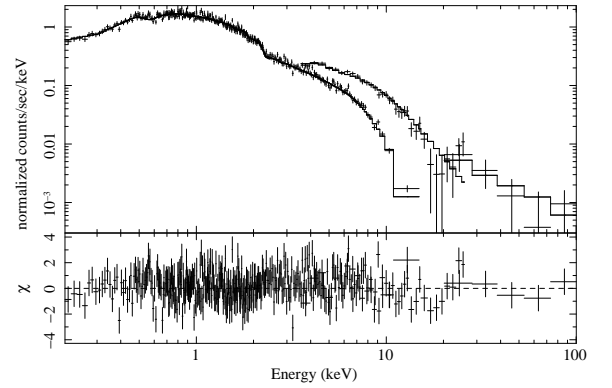


Fig. 9. The broad-band average X-ray spectrum of XSS J1227 using the *XMM-Newton* EPIC-pn, the *RXTE* PCA and *INTEGRAL* ISGRI spectra, fitted with a simple absorbed power law. The residuals are plotted in the lower panel.

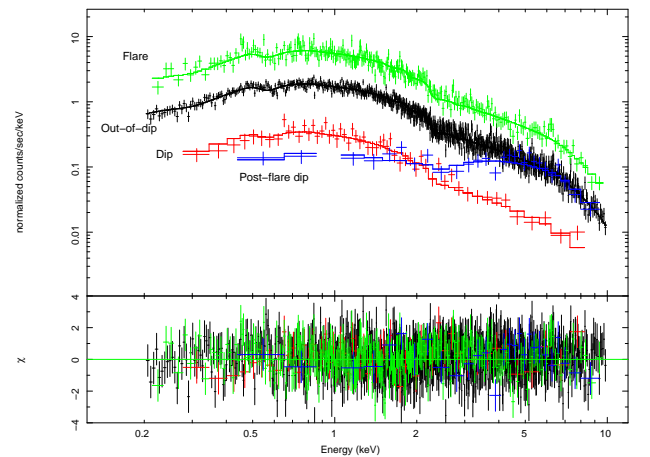


Fig. 10. Time-resolved *XMM-Newton* EPIC-pn spectra of XSS J1227 fitted with a simple absorbed power law. The post-flare dip spectral fit also includes a partial covering absorber. The lower panel shows the residuals

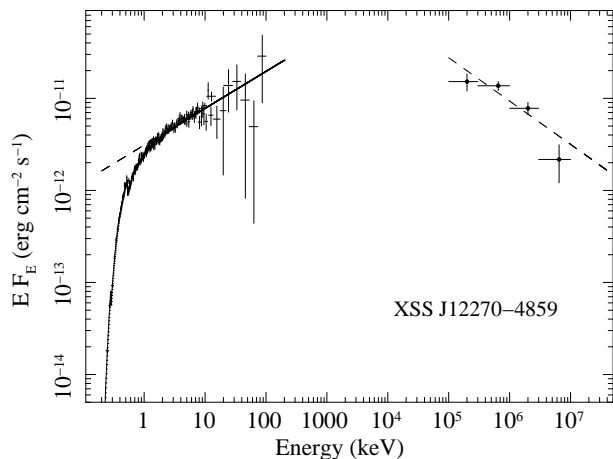


Fig. 11. The broad band X-ray to high energy gamma ray spectrum combining the *XMM-Newton* EPIC-pn, the *RXTE* PCA and *INTEGRAL* ISGRI rebinned data and the *Fermi* LAT data together with their respective best fit power law models. Solid line and dashed lines represent the absorbed and unabsorbed best fit spectral models.

those in the *XMM-Newton* EPIC-pn, *RXTE* PCA and *INTEGRAL* ISGRI bands. The energy spectrum is shown in Fig. 11 together with the corresponding best fit models with power law indexes 1.70 (low energy, Table 2) and 2.45 (high energy, sect.2). The shape of the combined spectrum suggests that if the low and high energy emissions are related, the peak energy should be between 1-100 MeV. A similar spectrum is observed in LS I+61°303; (Chernyakova et al. 2009), though it could be modeled under the assumption of a pulsar powered source. Lacking of knowledge on the nature of the source, it is not possible to use physical models at this stage. With our measured flux values, the 0.1-100 GeV/0.2-100 keV luminosity ratio is of the order of ~ 0.8 . Hence, if the identification is correct, the GeV emission is a significant component of the total energy output.

7. Discussion

We have presented X-ray, UV and optical/nIR observations of XSS J1227. We also found strong indication that this source has a high energy GeV counterpart as detected by the *Fermi* satellite. XSS J1227 shows remarkable large amplitude variability from X-rays to optical/near-IR. However, we did not detect the claimed 859.6 s periodicity in any data set from X-rays to UV/optical and near-IR ranges. The *XMM-Newton* X-ray light curve is characterized by short aperiodic variations consisting of flares and dips. The latter are observed during quiescence as well as immediately after the flares. This peculiar behaviour is also detected in a *Suzaku* observation (Saitou et al. 2009) carried out five months before the *XMM-Newton* pointing. This is not reported to be present in the *RXTE* observations performed in 2007 by Butters et al. (2008), but a re-analysis of the same data reveals instead a similar behaviour as detected by *XMM-Newton* and *Suzaku*. Also, the purported 859.6 s period is not detected in the same *RXTE* data. The broad-band X-ray spectrum is essentially featureless and is well described by an absorbed simple power law with $\Gamma \sim 1.6$. An emission feature at 6.2 keV could be present during flares. From both temporal and spectral characteristics, we therefore conclude that XSS J1227 is a persistent highly variable hard X-ray source that does not share any of the typical X-ray characteristics of magnetic CVs, especially of the

IP type, and any commonality of CV flares as for instance seen in AE Aqr (Choi & Dotani 2006) or UZ For (Still & Mukai 2001) and AM Her (de Martino et al. 2002). A similar conclusion was drawn by Saitou et al. (2009).

The evolution of the X-ray events is rather similar consisting of flare-dip pairs where the duration and intensity of flare and associated dips appear correlated. While no spectral changes are observed during flares with respect to quiescence, the spectrum hardens during the post-flare dips. A dense ($N_H = 6.1 \times 10^{22} \text{ cm}^{-2}$) absorbing material covering about $\sim 86\%$ of the X-ray source is required to fit these dips. This is suggestive of a flow of cool material appearing after the flares. These flares also occur in the UV but with longer duration. The UV variations lag by more than 300 s the X-ray ones. The UV flux gets bluer during the flares than in quiescence. It is then possible that large amplitude, long term variations first affect the outermost parts of an accretion disc that are cooler and then propagate towards smaller radii. The UV decay is delayed suggesting that the UV is also affected by reprocessing of X-rays after the flare.

Pronounced aperiodic X-ray dips are observed when the source is in quiescence with no significant spectral changes. On the other hand, no dips are detected in the UV band suggesting that they originate from random occultations by material very close to the X-ray source.

New optical and near-IR photometry reveals large amplitude (up to 50%) variability. A periodicity at 4.32 hr is derived from the optical data. The modulation at this period is single peaked in the optical whilst it is double-humped in the near-IR band. A marginal evidence of a low (4%) amplitude variability at this period is also found in the X-ray and UV ranges. If this period is linked to the orbital binary period it implies that XSS J1227 is a Low Mass X-ray Binary (LMXRB). The near-IR double humped modulation could then be due to ellipsoidal variations from the non-spherical low-mass donor star. The amplitude is determined by the orbital inclination angle i of the binary (Gelino et al. 2001). If it is indeed the case the binary inclination: $i \gtrsim 60^\circ$. On the other hand eclipses are not observed suggesting $i < 75^\circ$. We also revised the optical spectrum presented in Masetti et al. (2006) and confirm the equivalent widths of major Balmer emission lines. We note however that due to the low spectral resolution, the He II (4686Å) line is blended with C III (4650). We then measure $E.W.(\text{He II}) = 4 \pm 1 \text{ \AA}$, thus being much weaker than previously measured. Hence, the H_β and He II E.W. ratio, when compared to that of CVs and LMXRBs (van Paradijs & Verbunt 1984) locates XSS J1227 between the two object class locii. Furthermore the X-ray to optical flux ratio ranges between 48 (flares) and 17 (quiescence). This value is larger than that of CVs and magnetic systems and lies in the low value range of LMXRBs.

If XSS J1227 has an orbital period of 4.3 hr the donor is expected to be a low mass star with $M_2 \sim 0.3-0.4 M_\odot$ (Smith & Dhillon 1998; Pfahl et al. 2003; Knigge 2006) of spectral type between $\sim M3.1-M3.3$ and with an absolute near-IR J band magnitude $M_J \sim 6.7$ mag (Knigge 2006). The faintest measured J-band magnitude of XSS J1227 (16.9 mag), when corrected for interstellar absorption, $A_J = 0.12$ mag, obtained using the derived hydrogen column density from X-ray spectra, would imply a distance $d \gtrsim 1.1$ kpc, if the near-IR emission is totally due to the secondary star. This minimum distance could be consistent with the presence of near-IR ellipsoidal variations. Also, the source is located at $\sim 13^\circ$ in galactic latitude and, if it is in the galactic disc, its distance should not be exceedingly large. The X-ray bolometric luminosity is then $L_X \gtrsim 6 \times 10^{33} \text{ erg s}^{-1}$ suggesting a LMXRB accreting at a low rate.

The present analysis therefore favours XSS J1227 as a peculiar, low-luminosity LMXRB. Its flaring characteristics, consisting of flare-dip pairs are reminiscent of the type II bursts observed in the bursting pulsar GRO J1744-28 (Nishiuchi et al. 1999) or in the Rapid Burster (Lewin et al. 1996). However in these sources the energetics and timescales are much different as well as the spectral dependence of their associated dips. GRO J1744-28 could be more similar to XSS J1227, as the bursts (giant and small) do not show significant changes in spectral shape and show a good correlation between burst fluence and flux deficiency in the associated dips (Nishiuchi et al. 1999). However during the post-flare dips, GRO J1744-28 shows no spectral changes and the burst fluence is related to the time when the source is in the persistent quiescent state. This is not the case of XSS J1227. The Rapid Burster, instead shows different spectral behaviour during the post-flare dips as well as the pre-flare ones (Lewin et al. 1996). Hence, XSS J1227 could share common properties with type II bursts of the above sources, but with some differences.

Type II bursts are believed to be due to instabilities in the accretion disc that produce a rapid accretion onto the compact object depleting a reservoir in the inner disc regions. This is replenished immediately after the burst, thus producing a flux depression that does not affect the X-ray spectrum. However, type II bursts have not always the same morphology. For instance SMC X-1, a high mass X-ray binary, does not show post-flare dips (Angelini et al. 1991; Moon et al. 2003). Given the few sources known so far we cannot exclude that XSS J1227 is a type II low-level bursting source. Its UV activity starts before that in the X-rays. Also, the timescale of UV and X-ray flares is longer than that observed in the type II bursters and of the order of the free fall time $t_{\text{ff}} \gtrsim 603 (M_1/M_{\odot})^{-1/2}$ s from the Roche-lobe radius of the compact object ($R_{L,1} \gtrsim 0.66 R_{\odot}$ for $q = M_2/M_1 \leq 0.8$, for a $P_{\text{orb}} = 4.32$ hr and $M_2 \gtrsim 0.3 - 0.4 M_{\odot}$). The further presence of a partial (almost total) covering absorber during the post-flare dips could be the result of the replenishing of a larger portion of the accretion disc. This could be corroborated by the relatively long ($\sim 300-600$ s) post-flare dips.

While dips during quiescence are observed in many LMXRBs such as EXO 0748-676 (Bonnet-Bidaud et al. 2001) or 4U 1916-05 (Callanan 1993), these occur at specific orbital phases and are accompanied by a hardening of the source due to absorption of matter from the outer rim of the disc. XSS J1227 is hence different from the LMXRB dippers.

Type II bursters and LMXRB dippers are known to harbour a neutron star being either pulsars (SMC X-1 and GRO J1744) or also showing type I bursts, as the Rapid Burster, that are a signature of thermonuclear flashes on a neutron star. With the present data it is not possible to establish whether the compact object in XSS J1227 is a pulsar.

The *Fermi* detection in the GeV range of the source 1FGL J1227.9-4852, consistent with the XSS J1227 position, may further strengthen the interpretation of a LMXRB. Worthnoticing is that only a few X-ray binaries are detected so far with *Fermi*. In the first release of the *Fermi* source catalogue, only three are classified as High Mass X-ray Binaries (HMXRB) and five as LMXRBs, but among them three are associated with globular clusters, the other two are identified with the Galactic centre and the supernova remnant G332.4-00.4. The sources unambiguously identified by their periodicities are the HMXBs, 1FGL J0240.5+6116 (LS I+61°303; (Abdo & Fermi LAT Collaboration 2009a)), 1FGL J1826.2-1450 (LS 5039; (Abdo & Fermi LAT Collaboration 2009b)) and 1FGL J2032.4+4057 (Cyg X-3;

(Abdo & Fermi LAT Collaboration 2009c)). LS I+61°303 ($P_{\text{orb}}=26.5$ d) and LS 5039 ($P_{\text{orb}}=3.9$ d) are long period systems for which the high energy gamma ray emission dominates with rather similar $(0.1-100 \text{ GeV})/(0.2-100 \text{ keV})$ luminosity ratio of ~ 6.8 and ~ 6.2 , respectively; while for the shorter period system Cyg X-3 ($P_{\text{orb}}=0.2$ d) this ratio is at much lower value of $\sim 0.01-0.03$ ². With a value of ~ 0.8 , XSS J1227 could therefore be an intermediate system between these two regimes.

It is also possible that 1FGL J1227.9-4852 is a separate confusing source, like a Geminga-like pulsar. This possibility should not be discarded until a detailed temporal analysis of the GeV emission is performed. This will allow to infer whether a flaring-type activity on similar timescale as that observed in the X-rays and/or a periodic variability, either at the putative orbital period or neutron star spin, can be detected.

We also searched for a radio counterpart in the RADIO (Master Radio) catalogue available at HEASARC archive³. The only radio source within the 6' *Fermi* LAT error radius is catalogued in the Sydney University Molonglo Sky Survey, SUMSS J122820-485537 with a 843 MHz flux of 82.2 ± 2.7 mJy. This source, also shown in Fig. 1, is found at 5.22' from 1FGL J1227.9-4852 and at 4.12' from the XSS J1227 optical position. The radio positional accuracy is quite high with an ellipse uncertainty semi-major axis of 4.3" and semi-minor axis of 4.0". Hence, although within the *Fermi* LAT 95% confidence region, the association to XSS J1227 is quite unsecure.

The data presented here have therefore shown that XSS J1227 is a rather atypical LMXRB, that might reveal a new class of low-luminosity X-ray binaries or a peculiar accretion regime. The possible association with the GeV *Fermi* LAT source 1FGL J1227.9-4852 further suggests such peculiarity. To shed light into its intriguing nature a timing analysis of the high energy emission is essential for a secure identification with XSS J1227. Also, a long-term X-ray monitoring to constrain the flaring and dipping behaviour and to infer whether this source undergoes higher states or bursts is needed as well as time-resolved spectroscopy of the optical counterpart to confirm whether the photometric period is the binary orbital period.

Acknowledgements. DdM, TB and NM acknowledge financial support from ASI under contract ASI/INAF I/023/05/06 and ASI/INAF I/088/06/0 and also from INAF under contract PRIN-INAF 2007 N.17. We gratefully acknowledge the help of E. Bonning in the extraction of counts map from the *Fermi* LAT archive.

References

- Abdo, A. & Fermi LAT Collaboration. 2009a, *ApJ*, 701, 123
 Abdo, A. & Fermi LAT Collaboration. 2009b, *ApJ*, 706, 56
 Abdo, A. & Fermi LAT Collaboration. 2009c, *Science*, 325, 840
 Angelini, L., Stella, L., & White, N. 1991, *ApJ*, 371, 332
 Bonnet-Bidaud, J.-M., Haberl, F., Ferrando, P., Bennie, P., & Kendziorra, E. 2001, *A&A*, 365, 282
 Bradt, H., Rothschild, R., & Swank, J. 1993, *A&AS*, 97, 355
 Butters, O. W., Norton, A. J., Hakala, P. J., Mukai, K., & Barlow, E. 2008, *A&A*, 487, 271
 Callanan, P. 1993, *PASP*, 105, 961
 Chernyakova, M., Neronov, A., & Walter, R. 2009, *MNRAS*, 372, 1585
 Choi, C. & Dotani, T. 2006, *ApJ*, 646, 1149
 Conconi, P., Cuniffe, R., & D'Alessio, F. e. 2004, in *Proc. SPIE*, Vol. 5492, Ground-based Instrumentation for Astronomy, ed. F. M. Moorwood & I. Masanori, 1602
 de Martino, D., Matt, G., Gänsicke, B., et al. 2002, *A&A*, 396, 213

² The broad-band 0.2–100 keV fluxes of LS I+61°303, LS 5039 and Cyg X-3 are taken from Chernyakova et al. (2009), Takahashi et al. (2009) and Hjalmarsdotter et al. (2009), respectively.

³ <http://www.heasarc.gsfc.nasa.gov/W3Browse/all/radio.html>

- Dickey, J. M. & Lockman, F. J. 1990, *ARA&A*, 28, 215
- Gelino, D., Harrison, T., & McNamara, B. 2001, *AJ*, 122, 971
- Goldwurm, A., David, P., Foschini, L., et al. 2003, *A&A*, 411, L223
- Hjalmarsdotter, L., Zdziarski, A., Szostek, A., & Hannikainen, D. 2009, *MNRAS*, 392, 251
- Knigge, C. 2006, *MNRAS*, 373, 484
- Lebrun, F., Leray, J. P., Lavocat, P., et al. 2003, *A&A*, 411, L141
- Lewin, W., Rutledge, R., Kommers, J., van Paradijs, J., & Kouveliotou, C. 1996, *ApJ*, 462, 39
- Masetti, N., Morelli, L., Palazzi, E., et al. 2006, *A&A*, 459, 21
- Mason, K. O., Breeveld, A., Much, R., et al. 2001, *A&A*, 365, L36
- Moon, D., Eikenberry, S., & Wasserman, M. 2003, *ApJ*, 582, 91
- Nishiuchi, M., Koyama, K., Maeda, Y., et al. 1999, *ApJ*, 517, 436
- Pfahl, E., Rappaport, S., & Podsiadlowski, P. 2003, *ApJ*, 507, 1036
- Pretorius, M. 2009, *MNRAS*, 395, 386
- Saitou, K., Tsujimoto, M., Ebisawa, K., & Ishida, M. 2009, *PASJ*, 61
- Sazonov, S. & Revnivtsev, M. 2004, *A&A*, 423, 469
- Smith, D. & Dhillon. 1998, *MNRAS*, 301, 767
- Still, M. & Mukai, K. 2001, *ApJ*, 562, 71
- Strüder, L., Briel, U., Dennerl, K., et al. 2001, *A&A*, 365, L18
- Takahashi, T., Kishishita, T., Uchiyama, Y., & et al. 2009, *ApJ*, 697, 592
- Tosti, G., Bragaglia, M., & Campeggi, C. e. 2004, in *Proc. SPIE*, Vol. 5492, Ground-based Instrumentation for Astronomy, ed. F. M. Moorwood & I. Masanori, 689
- Turner, M. J. L., Abbey, A., Arnaud, M., et al. 2001, *A&A*, 365, L27
- Ubertini, P., Lebrun, F., Di Cocco, G., et al. 2003, *A&A*, 411, L131
- van Paradijs, J. & Verbunt, F. 1984, in *AIP Conf. Ser.*, Vol. 115, High Energy transients in Astrophysics, ed. S. E. Woosley, 49
- Zerbi, F., Chincarini, G., & Ghisellini, G. e. a. 2004, in *Proc. SPIE*, Vol. 5492, Ground-based Instrumentation for Astronomy, ed. F. M. Moorwood & I. Masanori, 1590